Journal of Magnetism and Magnetic Materials 487 (2019) 165241

Contents lists available at ScienceDirect

Journal of Magnetism and Magnetic Materials

journal homepage: www.elsevier.com/locate/jmmm

Research articles

Multiscale approaches for magneto-elasticity in device simulation

Laurent Bernard[a,*], Benjamin Joseph Mailhé[a], Nelson Sadowski[a], Nelson Jhoe Batistela[a], Laurent Daniel[b]

[a] GRUCAD/EEL/CTC, Universidade Federal de Santa Catarina, Florianópolis 88040-900, Brazil
[b] GeePs—Group of Electrical Engineering-Paris, UMR CNRS 8507, CentraleSupélec, Univ. Paris-Sud, Université Paris-Saclay, Sorbonne Université, 3 rue Joliot-Curie, Plateau de Moulon 91192 Gif-sur-Yvette CEDEX, France

ARTICLE INFO

Keywords:
Magneto-elastic behaviour
Multiscale modelling
Device simulation
Magnetic field analysis

ABSTRACT

Magnetoelastic couplings in ferromagnetic materials can be modelled using multiscale approaches. Various degrees of sophistication are accessible depending on the foreseen material and application. Here, we present a set of models, built on this approach, which can be used for devices magnetic field analysis. The representation of combined crystal anisotropy and texture effects is analysed through the introduction of a simplified fiber texture. A method is also proposed for the computation of magnetostriction hysteresis together with magnetization by association with a Jiles-Atherton model. All the models are detailed with their main physical and numerical characteristics, and the whole set of features that are needed for their use in device simulation tools. A test structure is finally simulated using the finite element method in order to illustrate the possibilities offered by these multiscale approaches.

1. Introduction

Magnetic and elastic properties are strongly coupled in ferromagnetic materials. This coupling may have uncontrolled side effects in some applications (e.g. variation of losses induced by mechanical stress [1,2], vibration induced by magnetostriction in electrical machines [3] or transformers [4,5]) or may be used advantageously in some others (e.g. magnetostrictive actuators [6,7], sensors [8,9], field weakening in permanent magnet synchronous machines [10]).

Simple models based on phenomenological assumptions are able to partially reproduce this complex coupled behaviour. For example, an extension of the well-known Jiles-Atherton hysteresis model, originally proposed by Sablik et al. [11], allows influencing the magnetic response of a material depending on an applied external stress thanks to the definition of a stress contribution to the effective magnetic field. Such model, even if interesting due to its simple formulation and implementation, suffers a narrow application range: indeed, 2- and 3-dimensional stress configurations need to be represented in a unidirectional fashion using equivalent stress formulations [12]. Moreover, the quality of obtained results is highly dependent on the available experimental data necessary to optimize the model [13]. Identical drawbacks are encountered in Preisach model adaptations. Because of these difficulties, this kind of stress dependent hysteresis model was rarely applied to magnetic field analysis simulations and only a few attempts were performed on simple structures [14,15].

The variety of configurations appearing in real-life devices and the difficulties associated with the full experimental characterization makes the use of more predictive models of utmost importance. Because mechanical stress and magnetic field should be represented, respectively, as a second order tensor and a vector, and because of strong non-linearities, the fully coupled magneto-elastic behaviour is very complex. In particular, magneto-elastic properties (permeability, hysteresis losses, magnetostriction) drastically change between uniaxial [16] and multiaxial [17–19] field/stress configurations. Possible ways to model the magneto-elastic macroscopic behaviour, in a multiaxial context, are know as energetic [20,21] and multiscale approaches [22–26]. These approaches are based on the material energy balance and give robust predictive models. Multiscale approaches aim at minimizing the potential energy resulting from the magnetic domain orientations. They also make use of transition rules between magnetic domain, single crystal and polycrystal scales. The resulting 3-scale model is very powerful to represent magneto-elastic behaviour in complex configurations. However, it is usually too demanding in terms of computation resources to be used for the simulation of devices.

Different simplifications of the anhysteretic multiscale approach can be considered and may lead to a variety of simplified multiscale models (SMSMs). Some of these SMSMs have already been analysed and applied to device simulations [2,5,27]. In this paper we make a synthesis

* Corresponding author.
E-mail address: laurent.bernard@ufsc.br (L. Bernard).

https://doi.org/10.1016/j.jmmm.2019.04.093
Received 7 January 2019; Received in revised form 14 March 2019; Accepted 26 April 2019
Available online 04 May 2019

on the available multiscale approaches and we highlight the specificities of each SMSM in terms of magneto-elastic behaviour representation and numerical evaluation. We also propose a new SMSM variant taking into account a simplified texture which is able to capture additional macroscopic characteristics of ferromagnetic materials. Some practical questions, raising when trying to couple these SMSMs to any device simulation method (integration, differentiation and inversion of the model), are addressed. A SMSM is then associated with the Jiles-Atherton model of magnetization hysteresis and we propose a method to obtain the corresponding magnetostriction hysteresis. Finally, we show an example of application using the finite element method to simulate the test structure defined in TEAM workshop problem 32 [28] and calculate the distribution of hysteretic induction and magnetostriction under mechanical stress and magnetic field.

2. Simplified multiscale approaches

Some characteristics of the full multiscale approach [22–25] cannot be preserved for application in device simulation. The main simplification which is common to all SMSMs presented here consists in neglecting local variations of the magnetic field and mechanical stress at the grain and domain scales. This means that the magnetic field and mechanical stress felt by magnetic domains are the same as the ones applied at macroscopic scale. In the full multiscale approach, a localization process [23] allows evaluating the loading at the grain scale. In the SMSMs, this step is avoided which reduces drastically the computation cost. Another assumption concerns the grain texture of the material. In the full multiscale approach the texture is represented in a rather precise way using data from EBSD (electron backscatter diffraction) measurements and accounting for a large set of grain orientations. In SMSMs, although some grains may be considered, the set of orientations must be reduced.

2.1. General approach at crystal scale

A crystal is considered as a set of magnetic domain families (domains with the same orientation) which volume fraction depends on the associated energy. At the scale of a magnetic domain, the local magnetization ($\vec{M}_\alpha$) and magnetostriction strain ($\boldsymbol{\varepsilon}_\alpha^\mu$) depend only on the direction $\vec{\alpha}$ (unit vector), the saturation magnetization (M_s) and maximum magnetostrictive strain constants (λ_{100} and λ_{111}):

$$\vec{M}_\alpha = M_s \vec{\alpha} \tag{1}$$

$$\boldsymbol{\varepsilon}_\alpha^\mu = \frac{3}{2}\begin{bmatrix} \lambda_{100}\left(\alpha_1^2 - \frac{1}{3}\right) & \lambda_{111}\alpha_1\alpha_2 & \lambda_{111}\alpha_1\alpha_3 \\ \lambda_{111}\alpha_2\alpha_1 & \lambda_{100}\left(\alpha_2^2 - \frac{1}{3}\right) & \lambda_{111}\alpha_2\alpha_3 \\ \lambda_{111}\alpha_3\alpha_1 & \lambda_{111}\alpha_3\alpha_2 & \lambda_{100}\left(\alpha_3^2 - \frac{1}{3}\right) \end{bmatrix} \tag{2}$$

where (α_1, α_2, α_3) are the components of vector $\vec{\alpha}$ in the chosen coordinate system. The potential energy (per unit volume) associated with one orientation is assumed to be the sum of magnetic, magneto-elastic and anisotropy contributions:

$$W_\alpha = W_\alpha^{mag} + W_\alpha^{el} + W_\alpha^{an} \tag{3}$$

with

$$W_\alpha^{mag} = -\mu_0 \vec{H}\cdot\vec{M}_\alpha \tag{4}$$

$$W_\alpha^{el} = -\boldsymbol{\sigma}\colon \boldsymbol{\varepsilon}_\alpha^\mu \tag{5}$$

and W_α^{an} may depend on further assumptions related to each SMSM. In these equations, μ_0 is the vacuum permeability, $\vec{H}$ is the applied magnetic field and $\boldsymbol{\sigma}$ is the applied stress. The scalar product of vectors $\vec{a}$ and $\vec{b}$ is $\vec{a}\cdot\vec{b} = \Sigma_{i=1}^3 a_i b_j$ and the double-dot product of second order tensors $\boldsymbol{a}$ and $\boldsymbol{b}$ is $\boldsymbol{a}\colon\boldsymbol{b} = \Sigma_{i=1}^3\Sigma_{j=1}^3 a_{ij} b_{ij}$. The volume fraction of each domain family (domains with the same orientation $\vec{\alpha}$) is then calculated considering a Boltzmann statistics [22] as

$$f_\alpha = \frac{\exp(-A_s W_\alpha)}{\int \exp(-A_s W_\alpha) d\alpha} \tag{6}$$

where A_s is a parameter of the SMSM which can be related to the permeability at zero field [24]. Finally, the anhysteretic magnetization and magnetostriction strains at the crystal scale are obtained by the weighted sum over all possible directions

$$\vec{M} = \langle \vec{M}_\alpha \rangle = \int f_\alpha \vec{M}_\alpha \, d\alpha \tag{7}$$

$$\boldsymbol{\varepsilon}^\mu = \langle \boldsymbol{\varepsilon}_\alpha^\mu \rangle = \int f_\alpha \boldsymbol{\varepsilon}_\alpha^\mu \, d\alpha \tag{8}$$

Along the text, character α is used as a subscript for any quantity associated with a specific domain orientation (denoted by unit vector $\vec{\alpha}$). The notation $d\alpha$ is merely used to indicate that the integrals are performed over the set of possible domain orientations. Numerically, these integrals are evaluated by discrete sums considering a finite number of possible domain orientations [29].

The general approach presented here, for the determination of magnetization and magnetostriction at the crystal scale, can be used in different ways to represent the macroscopic behaviour of a material. Some possibilities are shown in the following Sections 2.2 and 2.3. The main differences between these approaches consist in the definition of the anisotropy, the set of possible domain orientations and the set of crystal orientations that may be considered.

2.2. Macroscopically equivalent single crystal

This kind of SMSM aims at representing the macroscopic behaviour from a unique equivalent crystal.

2.2.1. Analytical model

Analytical expressions of the magnetization and magnetostriction can be obtained for isotropic materials by reducing the number of possible domain orientations to 6 [30,31]. An orthonormal basis ($\vec{h}$, $\vec{p}$, $\vec{z}$) associated with the magnetic field is considered. The unit vector $\vec{h}$ represents the direction of the magnetic field, $\vec{z}$ is an arbitrary unit vector perpendicular to the magnetic field and $\vec{p} = \vec{z} \times \vec{h}$ completes the basis. The set of possible domain orientations is then defined as $\{\vec{h}, -\vec{h}, \vec{p}, -\vec{p}, \vec{z}, -\vec{z}\}$. The isotropic crystal is obtained by setting $W_\alpha^{an} = 0$ and $\lambda_{100} = \lambda_{111} = \lambda_s$. This last condition leads to the isotropic local magnetostriction tensor:

$$\boldsymbol{\varepsilon}_\alpha^\mu = \frac{3}{2}\lambda_s\left(\vec{\alpha}\otimes\vec{\alpha} - \frac{1}{3}\boldsymbol{I}\right) \tag{9}$$

where $\otimes$ represents the tensor product and $\boldsymbol{I}$ is the 2nd-order identity tensor. The magnetization and magnetostriction are then:

$$\vec{M} = \frac{A_h sinh(\kappa H)}{A_h cosh(\kappa H) + A_p + A_z} M_s \vec{h} \tag{10}$$

$$\boldsymbol{\varepsilon}^\mu = \lambda\left(\vec{h}\otimes\vec{h} - \frac{1}{2}(\vec{p}\otimes\vec{p} + \vec{z}\otimes\vec{z})\right) \tag{11}$$

with

$$\lambda = \lambda_s\left(1 - \frac{3}{2}\frac{A_p + A_z}{A_h cosh(\kappa H) + A_p + A_z}\right) \tag{12}$$

and

$$A_i = exp(\tau\sigma_{ii}) \tag{13}$$

for $i \in \{h, p, z\}$, where σ_{ii} is the ii-component of the applied stress tensor. Two constants are defined as $\kappa = \mu_0 A_s M_s$ and $\tau = (3/2)A_s\lambda_s$. The analytical model offers simple expressions for the magneto-elastic

behaviour and retains the effects of multiaxial stress (normal stresses with respect to the chosen basis). The variation of domain volume fractions with the magnetic field can be interpreted as a consequence of domain wall motion only. No domain rotation effect can be represented as crystal anisotropy is not considered and as the model always includes domains parallel to the magnetic field. Shear stress effects with respect to the chosen basis are also neglected. The model does not incorporate intrinsic anisotropy, and magnetization and magnetostriction always follow the magnetic field orientation. However induced anisotropy is accounted for as the behaviour depends on the relative orientation of the magnetic field and mechanical stress tensor.

2.2.2. Discrete model

In this approach the set of possible domain orientations does not depend on the magnetic field. The set is defined from a discretization of the unit sphere. In order to avoid uncontrolled anisotropy effects, the set should be as dense and uniform as possible [29]. To this purpose the nodes of an icosphere can be used. An icosphere is a triangular mesh of the sphere built by regular subdivision of the triangular faces of an icosahedron. The set density is then determined by the icosphere order (number of subdivisions) and presents a central symmetry which ensures the existence of opposite orientation domain families and hence zero magnetization and magnetostriction when no magnetic field or stress is applied.

The main specificity of the discrete model relies on the treatment of anisotropy. For perfect single crystals, saturation magnetostriction constants and anisotropy energy constants are well defined and tabulated for many materials. There are, in fact, only two scales to be considered (the domain scale and the grain scale) and they are both represented by the model. In this case, for a cubic crystal, the anisotropy energy is [24]

$$W_\alpha^{an} = K_1(\alpha_1^2\alpha_2^2 + \alpha_2^2\alpha_3^2 + \alpha_3^2\alpha_1^2) + K_2\alpha_1^2\alpha_2^2\alpha_3^2 \tag{14}$$

where K_1 and K_2 are the anisotropy constants. For strongly textured materials (e.g. Goss texture materials), the macroscopic behaviour might be similar to the one of the single crystal. As a consequence, magnetostriction anisotropic tensor and anisotropy energy of the crystal can be used as a basis for the macroscopically equivalent single crystal. Some corrections can be applied in order to get a better representation of the true macroscopic behaviour, in particular if structure induced anisotropy has to be accounted for (demagnetizing field effects) [5]. Finally, for weakly textured materials, the strong anisotropy existing at the crystal scale is very different from the (generally weak) macroscopic anisotropy. In consequence, an equivalent single crystal can be defined considering an isotropic local magnetostriction tensor ($\lambda_{100} = \lambda_{111} = \lambda_s$) and adjusting the anisotropy energy in order to fit the macroscopic behaviour. The choice of an isotropic magnetostriction tensor implies that the material will have the same saturation magnetostriction for all directions. The macroscopic anisotropy might come from texture or structure effects. It can take different forms, e.g., $J\left(\vec{\alpha}\cdot\vec{\beta}\right)^2$ [27] for a uniaxial anisotropy where $\vec{\beta}$ is the anisotropy direction and J is the anisotropy constant, or $C\vec{\alpha}\cdot(\boldsymbol{N}\vec{\alpha})$ [5] for a multiaxial anisotropy where C is the anisotropy constant and $\boldsymbol{N}$ is a normalized diagonal matrix (in the coordinate system associated with the principal anisotropy axes). In such an approach for weakly textured materials, because microcrystalline anisotropy is not considered, the effects of domain rotations are not represented and the magnetization process can be interpreted in terms of domain wall motion only.

2.3. Macroscopically equivalent simplified texture

Some characteristics of the magneto-elastic behaviour cannot be represented by the SMSMs based on an equivalent single crystal. For example, the non-monotonous behaviour of the magnetostriction as a function of the magnetization or inflexions in the curve of magnetization against magnetic field remain out of reach for such models. These phenomena appear as consequences of material texture and strong crystal anisotropy. A possible way to retrieve this kind of behaviour consists in considering a simplified texture made of a few crystals only. Each crystal (or grain) is treated independently to compute the associated magnetization ($\vec{M}_g$) and magnetostriction ($\boldsymbol{\varepsilon}_g^\mu$) from Eqs. (7) and (8). The macroscopic behaviour is then calculated by a weighted sum over the grains. For this model, the magnetization and magnetostriction are redefined as

$$\vec{M} = \sum_g f_g \vec{M}_g \tag{15}$$

$$\boldsymbol{\varepsilon}^\mu = \sum_g f_g \boldsymbol{\varepsilon}_g^\mu \tag{16}$$

where the sum is made on all the grain orientations of the considered simplified texture, f_g represents the proportion of each grain orientation, and $\vec{M}_g$ and $\boldsymbol{\varepsilon}_g^\mu$ are the magnetization and magnetostriction given by the single crystal model.

As an example, the anhysteretic magneto-elastic behaviour of a non-oriented Fe-3%Si laminated material [32,17] is modelled using this approach. The measured texture data are presented as pole figures (Fig. 1). This texture is fairly similar to the one of a perfect ⟨111⟩ fibre with its axis perpendicular to the sheet plane (Fig. 2). Such a texture can be obtained (for modelling) starting from a crystal with a [111] direction perpendicular to the sheet plane and generating a set of crystals by rotations, with respect to this axis, of angles uniformly distributed between 0 and $2\pi/3$ (because of the periodicity of this configuration).

A simplified fibre made of only 4 crystals, in equal proportion (i.e. with $f_g = 0.25$), which pole figures is represented in Fig. 2 by rhombi, is analysed here. The model parameters and their values are presented in Table 1. These values are the same as in [32]. They come from tabulated references for all parameters except for A_s, which value is identified from the experimental initial susceptibility under no stress [24].

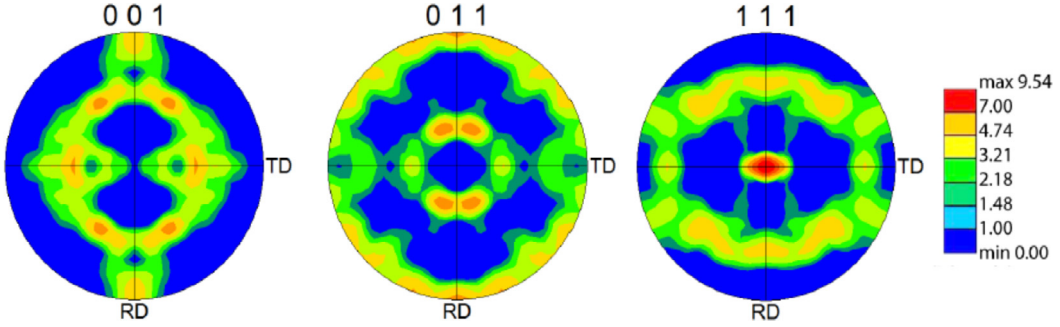

Fig. 1. Pole figures (stereographic projection) for non-oriented Fe-3%Si from [32].

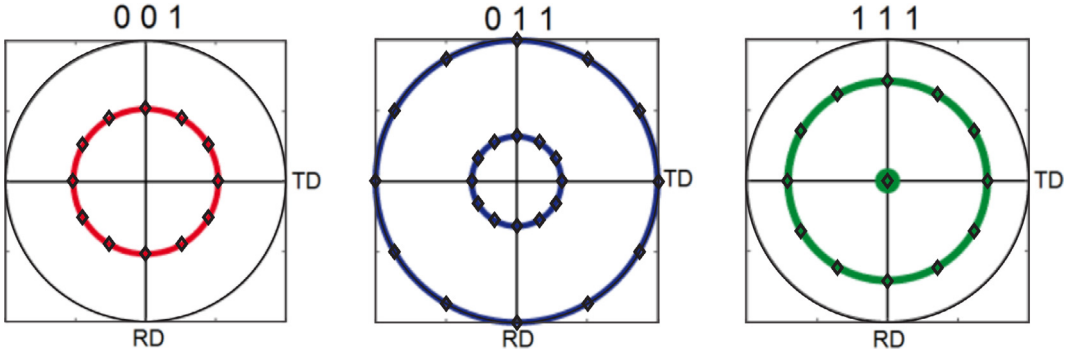

Fig. 2. Pole figures for a perfect ⟨111⟩ fibre with the axis perpendicular to the sheet plane.

Table 1
Parameters of the simplified texture SMSM for Fe-3%Si.

$A_s (m^3/J)$	$M_s (A/m)$	λ_{100}	λ_{111}
$3 \cdot 10^{-3}$	$1.6 \cdot 10^{6}$	$23 \cdot 10^{-6}$	$-4.5 \cdot 10^{-6}$
K_1 (kJ/m^3)	K_2 (kJ/m^3)		
38	0		

In the simplified approach presented here, optimization of these parameters could be done within a reasonable range and could help in fitting with experimental results. However, this kind of adjustment is not considered here, and we focus on showing that, from small set of tabulated values, the model is able to reproduce the main characteristics of the material behaviour. Magnetization and magnetostriction are analysed as functions of the direction of the applied magnetic field in the sheet plane. Fig. 3 and Fig. 4 show the envelopes of the set of curves obtained by varying the direction of the applied magnetic field from 0° to 90° (with respect to the RD) by 5° steps, when no stress is applied. These figures show that the model has a mainly isotropic behaviour. Some anisotropic behaviour (characterized by a wider envelope curve in Fig. 4) appears on magnetostriction near saturation due to the small set of crystals. For fibres made of more than 5 crystals this anisotropy would be hardly noticeable in these graphics. The component of magnetostriction perpendicular to the sheet plane (not presented here) is less than 1% of the other components below saturation ($M < 1.3 \cdot 10^6$ A/m) because the axis of the fibre is a ⟨111⟩ hard magnetization direction. The change of sign of the slope of magnetostriction curves observed when reaching saturation is an expected behaviour which results from the combination of different crystals with strong anisotropic properties. This kind of phenomenon cannot be reproduced by the simpler SMSMs presented in previous sections.

The effect of uniaxial stress (parallel to the magnetic field) is presented in Figs. 5–7: results from the model are on the left, experimental data from [32] are on the right. It should be noticed that magnetostriction curves are plotted using the saturation value as reference. In experimental results, because of the noise present on measurement, this may result in small uncontrolled vertical shifts. The model shows good consistency with experimental results. In particular, it can be noticed that it reproduces the inflexion of the magnetization curve which can be observed under strong compressive stress (−100 MPa). However, one characteristic of the real material behaviour cannot be represented by the model: the effect of tensile stress should be non-monotonous [17,18,32,33]. For the considered material, a tensile stress lower than 50 MPa increases the magnetization and reduces the variations of the magnetostriction strain, but starts to have the opposite effect at higher values. This experimental observation is not described by the model.

3. Integration, differentiation and inversion of the SMSM

In order to enable the use of SMSM models in device simulation tools, some important properties are detailed in this section. Integration of the model gives access to the energy stored in the material. Differentiation allows the application of differential time-stepping schemes and non-linear Newton-Raphson algorithms for the resolution. Finally, inverse models are needed for the implementation in the commonly used strain and magnetic flux density based formulations (such as the displacement and magnetic vector potential formulations).

For the sake of simplicity, the case of the numerical equivalent

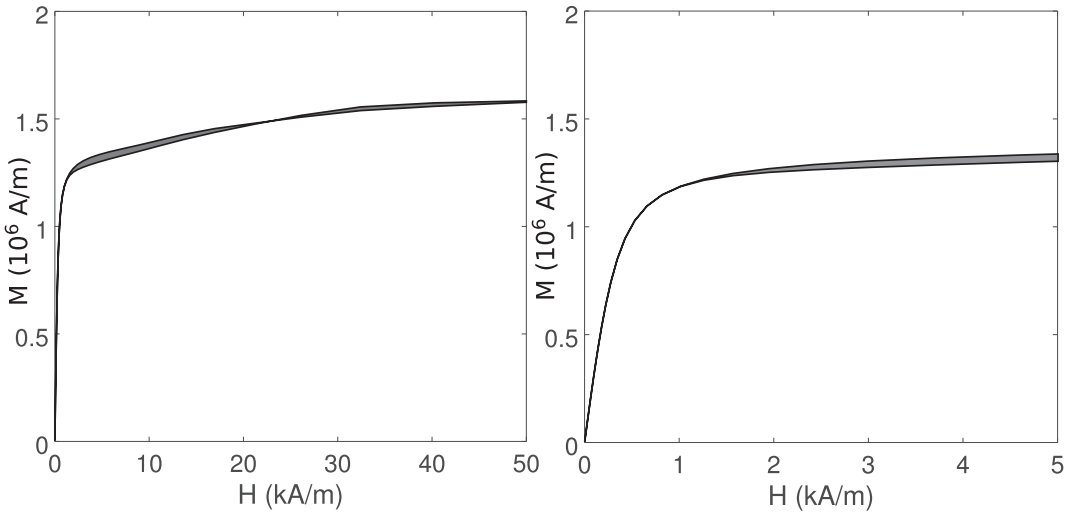

Fig. 3. Envelope curve of the parallel magnetization as a function of magnetic field, obtained by rotation of the magnetic field from 0° to 90° with respect to the RD (the right figure is a zoom on the *H*-axis of the left one).

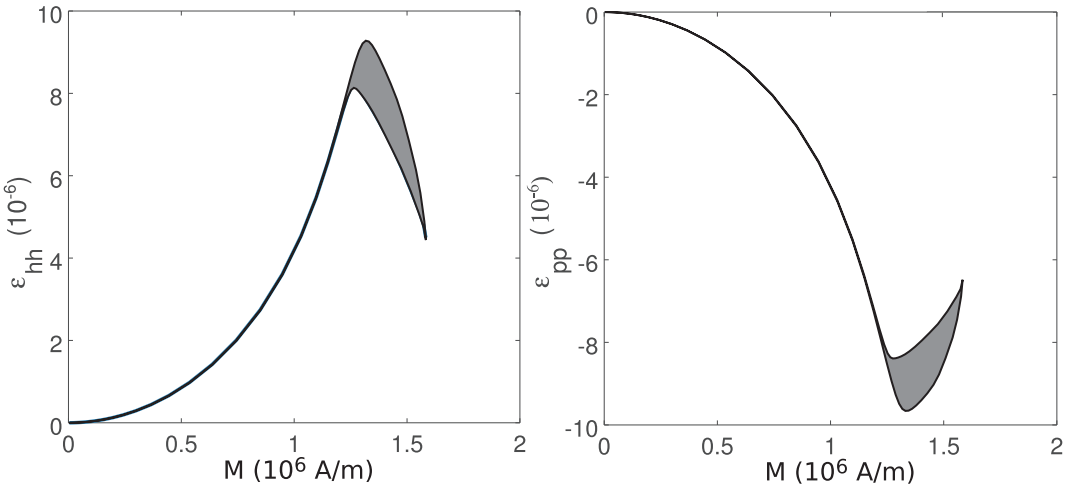

Fig. 4. Envelope curve of the parallel and perpendicular magnetostriction in the sheet plane as a function of magnetization, obtained by rotation of the magnetic field from 0° to 90° with respect to the RD.

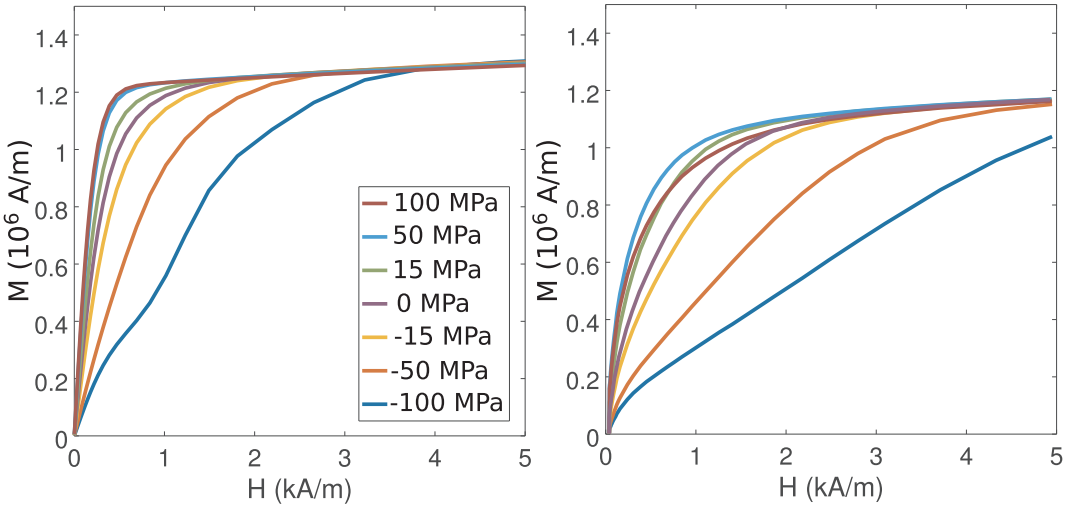

Fig. 5. Magnetization as a function of the magnetic field, for different values of the uniaxial stress: multiscale model with simplified texture (left), measurements (right) from [32].

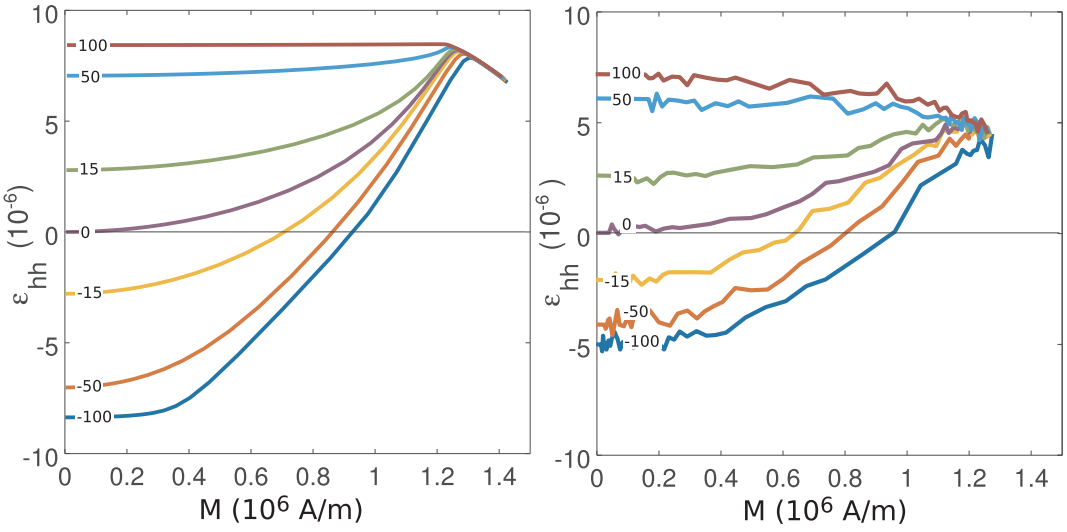

Fig. 6. Parallel magnetostriction (ϵ_{hh}) in the sheet plane as a function of magnetization, for different values of the uniaxial stress (in MPa): multiscale model with simplified texture (left), measurements (right) from [32].

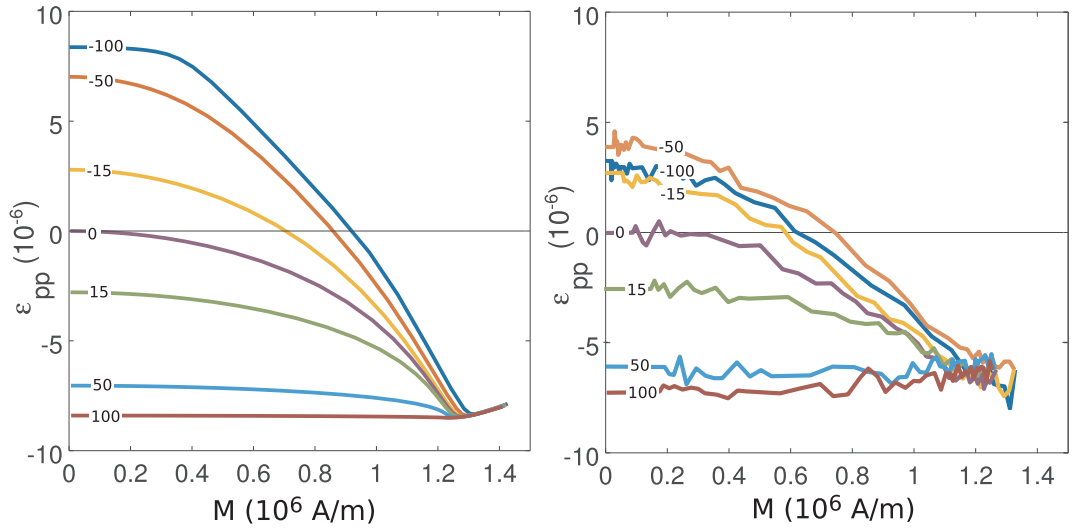

Fig. 7. Perpendicular magnetostriction (ϵ_{pp}) in the sheet plane as a function of magnetization, for different values of the uniaxial stress (in MPa): multiscale model with simplified texture (left), measurements (right) from [32].

single crystal SMSM is considered. All results can be straightforwardly extended to the equivalent simplified texture SMSM by applying weighted sum just as in Eqs. (15) and (16). The case of the analytical model is not fully treated but its specificities, which come from its magnetic field dependent local magneto-elastic energy, are highlighted in a separate section.

3.1. Integration

The total magneto-elastic co-energy density of an anhysteretic material can be defined as

$$w_c = \int \vec{B} \cdot d\vec{H} + \int \boldsymbol{\varepsilon} : d\boldsymbol{\sigma} \tag{17}$$

where $\vec{B}$ and $d\vec{H}$ are vectors, and $\boldsymbol{\varepsilon}$ and $d\boldsymbol{\sigma}$ are second order tensors. The integrals on $\vec{H}$ and $\boldsymbol{\sigma}$ are calculated between a reference state, which might be ($\vec{H} = \vec{0}$, $\boldsymbol{\sigma} = \mathbf{0}$), and the current state, independently from the path between these two states. The magnetic flux density is $\vec{B} = \mu_0(\vec{H} + \vec{M})$ and the total strain is $\boldsymbol{\varepsilon} = (\boldsymbol{\varepsilon}^e + \boldsymbol{\varepsilon}^\mu)$, where $\boldsymbol{\varepsilon}^e$ is the elastic strain tensor. The *part* of the co-energy relative to the magneto-elastic behaviour is then

$$\int \mu_0 \vec{M} \cdot d\vec{H} + \int \boldsymbol{\varepsilon}^\mu : d\boldsymbol{\sigma} = \frac{1}{A_s} ln\left(\int exp(-A_s W_\alpha) d\alpha \right) \tag{18}$$

which can be verified by partial differentiation with respect to the magnetic field or the mechanical stress. The co-energy can then be calculated for any loading from the energy associated with each domain family. It can be noticed that the total energy density *is not* the mean value of the energies associated with each domain family ($\int f_\alpha W_\alpha d\alpha$), which means that the model implicitly includes interactions between domains. The energy density may be calculated from the co-energy density by

$$w = \vec{B} \cdot \vec{H} + \boldsymbol{\varepsilon} : \boldsymbol{\sigma} - w_c. \tag{19}$$

3.2. Differentiation

Magnetization ($\vec{M}$) and magnetostriction ($\boldsymbol{\varepsilon}$) can be differentiated with respect to the input variables, i.e. the magnetic field ($\vec{H}$) and the stress ($\boldsymbol{\sigma}$). We may start with the differential susceptibility tensor, which is the partial derivative of $\vec{M}$ with respect to $\vec{H}$ at constant stress $\boldsymbol{\sigma}$. Because $\vec{M}_\alpha$ and $\vec{\alpha}$ do not depend on the magnetic field, we have:

$$\partial_{\vec{H}} \vec{M} = \int \vec{M}_\alpha \otimes \partial_{\vec{H}} f_\alpha \, d\alpha \tag{20}$$

It can be shown [2,34] that the partial derivative of f_α with respect to $\vec{H}$ is:

$$\partial_{\vec{H}} f_\alpha = A_s f_\alpha \left(\int f_\alpha \partial_{\vec{H}} W_\alpha d\alpha - \partial_{\vec{H}} W_\alpha \right) \tag{21}$$

From Eq. (3)–(5), and considering that the anisotropy energy does not depend on magnetic field and stress, we also have:

$$\partial_{\vec{H}} W_\alpha = -\mu_0 \vec{M}_\alpha \tag{22}$$

Finally, the analytical expression for the differential susceptibility is obtained as:

$$\partial_{\vec{H}} \vec{M} = \mu_0 A_s \left(\int f_\alpha \vec{M}_\alpha \otimes \vec{M}_\alpha \, d\alpha - \vec{M} \otimes \vec{M} \right) \tag{23}$$

From Eq. (23), the differential susceptibility tensor appears to be proportional to the difference between the tensor product of the macroscopic magnetization by itself and the volume fraction weighted average of the tensor product of the local magnetization by itself. The other components of the differential model can be obtained in the same way:

$$\partial_{\boldsymbol{\sigma}} \boldsymbol{\varepsilon}^\mu = A_s \left(\int f_\alpha \boldsymbol{\varepsilon}_\alpha^\mu \otimes \boldsymbol{\varepsilon}_\alpha^\mu \, d\alpha - \boldsymbol{\varepsilon}^\mu \otimes \boldsymbol{\varepsilon}^\mu \right) \tag{24}$$

$$\partial_{\boldsymbol{\sigma}} \vec{M} = A_s \left(\int f_\alpha \vec{M}_\alpha \otimes \boldsymbol{\varepsilon}_\alpha^\mu \, d\alpha - \vec{M} \otimes \boldsymbol{\varepsilon}^\mu \right) \tag{25}$$

$$\partial_{\vec{H}} \boldsymbol{\varepsilon}^\mu = \mu_0 A_s \left(\int f_\alpha \boldsymbol{\varepsilon}_\alpha^\mu \otimes \vec{M}_\alpha \, d\alpha - \boldsymbol{\varepsilon}^\mu \otimes \vec{M} \right) \tag{26}$$

where $\partial_{\boldsymbol{\sigma}} \boldsymbol{\varepsilon}^\mu$ is a fourth order tensor, $\partial_{\boldsymbol{\sigma}} \vec{M}_{an}$ and $\partial_{\vec{H}} \boldsymbol{\varepsilon}^\mu$ are third order tensors. The last two tensors verify $\mu_0 (\partial_{\boldsymbol{\sigma}} \vec{M})_{ijk} = (\partial_{\vec{H}} \boldsymbol{\varepsilon}^\mu)_{jki}$ as they should, considering that they derive from the same co-energy and applying Schwarz theorem. The set of Eqs. (23)–(26) constitutes the output of the differential SMSM. In terms of components, the tensors appearing in Eqs. (23)–(25) are of the form:

$$(\partial_{\vec{H}} \vec{M})_{ij} = \frac{\partial M_i}{\partial H_j} \tag{27}$$

$$(\vec{M} \otimes \vec{M})_{ij} = M_i M_j \tag{28}$$

$$(\partial_{\boldsymbol{\sigma}} \boldsymbol{\varepsilon}^\mu)_{ijkl} = \frac{\partial \epsilon_{ij}^\mu}{\partial \sigma_{kl}} \tag{29}$$

$$(\boldsymbol{\varepsilon}^{\mu} \otimes \boldsymbol{\varepsilon}^{\mu})_{ijkl} = \epsilon^{\mu}_{ij}\epsilon^{\mu}_{kl} \tag{30}$$

$$(\partial_{\sigma}\vec{M})_{ijk} = \frac{\partial M_i}{\partial \sigma_{jk}} \tag{31}$$

$$(\vec{M} \otimes \boldsymbol{\varepsilon}^{\mu})_{ijk} = M_i\,\epsilon^{\mu}_{jk} \tag{32}$$

3.3. Inversion

Full inversion of the SMSM consists in allowing the magnetic flux density ($\vec{B}$) and the mechanical total strain ($\boldsymbol{\varepsilon}$) to be the input parameters (state variables) [35]. From the differential model, the inverse SMSM can be obtained numerically. Using Voigt notation for the stress and strain tensors, the differential model can be written in matrix form as:

$$\begin{bmatrix} \mu_0 d\vec{M} \\ d\boldsymbol{\varepsilon}^{\mu} \end{bmatrix} = \begin{bmatrix} \mu_0 \partial_{\vec{H}}\vec{M} & \mu_0 \partial_{\sigma}\vec{M} \\ \partial_{\vec{H}}\boldsymbol{\varepsilon}^{\mu} & \partial_{\sigma}\boldsymbol{\varepsilon}^{\mu} \end{bmatrix} \begin{bmatrix} d\vec{H} \\ d\boldsymbol{\sigma} \end{bmatrix} = \boldsymbol{F} \begin{bmatrix} d\vec{H} \\ d\boldsymbol{\sigma} \end{bmatrix} \tag{33}$$

To inverse the model, we need to find $(\vec{H}, \boldsymbol{\sigma})$ such that:

$$\vec{B} = \mu_0(\vec{H} + \vec{M}) \tag{34}$$

and

$$\boldsymbol{\varepsilon} = \boldsymbol{S}\colon \boldsymbol{\sigma} + \boldsymbol{\varepsilon}^{\mu} \tag{35}$$

where $\boldsymbol{S}$ represents the elastic compliance tensor. Using Newton–Raphson method, an approximate solution is found by solving iteratively:

$$\begin{bmatrix} \delta\vec{H} \\ \delta\boldsymbol{\sigma} \end{bmatrix} = -\boldsymbol{G}^{-1} \begin{bmatrix} \delta\vec{B} \\ \delta\boldsymbol{\varepsilon} \end{bmatrix} \tag{36}$$

where

$$\boldsymbol{G} = \begin{bmatrix} \mu_0 \boldsymbol{I}_1 & 0 \\ 0 & \boldsymbol{S} \end{bmatrix} + \boldsymbol{F} \tag{37}$$

and $\begin{bmatrix} \delta\vec{B} \\ \delta\boldsymbol{\varepsilon} \end{bmatrix}$ is the residual.

With the objective of analysing the convergence properties of the inverse model, we consider the case of the equivalent single crystal SMSM with a set of possible directions given by a 4-th order icosphere (2562 orientations). The iterative Newton-Raphson procedure is stopped when the relative variation of the norm of the magnetic flux density is less than 10^{-10} or when the algorithm starts diverging (in this case, values corresponding to the prior iteration are considered). The parameters used for the model are given in Table 2 and are meant to represent a typical non-oriented material. To illustrate the results, we show the map of the *xxx*-component of tensor $\partial_{\varepsilon}\vec{H}$ with respect to the $x-$ and $y-$components of the induction flux density obtained from the inverse model and the corresponding convergence characteristics (Fig. 8). The maps are obtained by nested loops incrementing each component of the magnetic flux density ($y-$component is incremented in the inner loop), starting from $\vec{B} = 0$ and using last solution as initial guess in the iterative process. The map of $(\partial_{\varepsilon}\vec{H})_{xxx}$ shows the expected material behaviour (this kind of map can be useful for the analysis of magneto-mechanical transducers [9]). The map of iteration number (Fig. 8 (b)) should be analysed together with the logarithm of the relative error on the norm of the magnetic flux density (Fig. 8 (c)). In the region where this norm is less than the convergence criterion (10^{-10}), the algorithm converges in less than 6 iterations. In the region where this norm is more than the convergence criterion (10^{-10}), the algorithm starts diverging at the second iteration generally. The logarithm of the Frobenius norm of the total displacement (Fig. 8 (c)) represents the absolute error on the second entry of the inverse model (the imposed total displacement being null, a relative error cannot be defined). This map shows that, when convergence is reached, the total displacement is small (less than 10^{-14}). The convergence difficulties encountered in highly saturated regions are linked with the discretization of the set of possible domain orientations, which impacts on the evaluation of integrals and induces small local anisotropies at high field intensities. The same maps are drawn in Fig. 9 using an icosphere of order 6 (40962 orientations), instead of order 4. In this case, the convergence is always reached. A kind of radial pattern, associated with the discretization, is noticeable in the upper-right corner of Fig. 9 (b).

This example shows that good convergence characteristics can be obtained by direct application of the Newton–Raphson procedure to inverse model, eventually refining the discretization of the possible domain orientations.

Table 2
Parameters for the equivalent model.

A_s (m^3/J)	M_s (A/m)	λ_s	J (J/m^3)
10^{-2}	$1.6{\cdot}10^6$	10^{-5}	0

3.4. Comments on the analytical SMSM

The magnetization of the analytical SMSM can be differentiated with respect to the magnetic field from Eq. (10). The component $(\partial_{\vec{H}}\vec{M})_{hh}$ was already presented in [30]. The calculation of the full differential susceptibility tensor is more complex. We just sketch here the calculus in order to highlight the main difficulties. The matrix representation of vectors and second order tensors is found more convenient and used here. First we can note

$$\boldsymbol{D} = \partial_{\vec{H}}\vec{h} = \frac{1}{H}(\boldsymbol{I} - \vec{h}\vec{h}'). \tag{38}$$

where $'$ is the transposition operator and $\boldsymbol{I}$ is the identity matrix. Then we write

$$\partial_{\vec{H}}\vec{M} = M\boldsymbol{D} + \vec{h}\,\partial_{\vec{H}}M \tag{39}$$

where $\partial_{\vec{H}}M$ is a row vector. To go further, we choose a vector $\vec{z}$ independent of the magnetic field and we define

$$\boldsymbol{D}_p = \partial_{\vec{H}}\vec{p} = \partial_{\vec{H}}\vec{z} \times \vec{h} = X_{\vec{z}}\boldsymbol{D} \tag{40}$$

where $X_{\vec{z}}$ is the antisymmetric matrix associated with the left vector product by $\vec{z}$. We also define

$$\vec{g}' = \partial_{\vec{H}}\sigma_{hh} = \partial_{\vec{H}}\vec{h}'\boldsymbol{\sigma}\vec{h} = 2\boldsymbol{D}\boldsymbol{\sigma}\vec{h}' \tag{41}$$

and similarly

$$\vec{g}_p' = \partial_{\vec{H}}\sigma_{pp} = (\boldsymbol{D}_p + \boldsymbol{D}_p')\boldsymbol{\sigma}\vec{p}\,' \tag{42}$$

Then we have

$$\partial_{\vec{H}}A_h = \tau\, exp(\tau\sigma_{hh})\vec{g}' \tag{43}$$

$$\partial_{\vec{H}}A_p = \tau\, exp\left(\tau\sigma_{pp}\right)\vec{g}_p' \tag{44}$$

and

$$\partial_{\vec{H}}A_z = \vec{0}' \tag{45}$$

which are needed to reach an explicit form of $\partial_{\vec{H}}M$, with some more straightforward but cumbersome work. The other blocks of the differential model would require significant additional efforts. The difficulties associated with the analytical SMSM rely on the fact that the local magneto-elastic energy depends on the applied magnetic field, and then (22) does not hold. The model retains only the principal stresses in the basis defined from the magnetic field direction, and they might change as the magnetic field rotates. In particular, pure shear stress in an initial

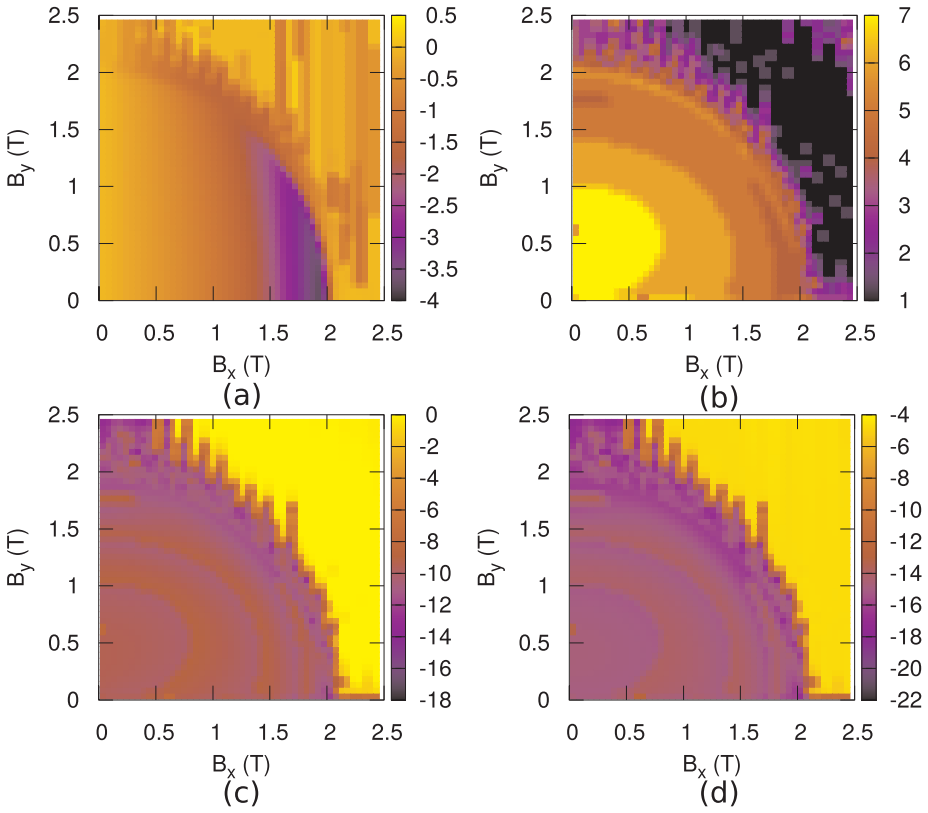

Fig. 8. Maps of (a) $(\partial_\epsilon \vec{H})_{xxx}$ (10^6 A/m), (b) number of converging iterations of the Newton–Raphson algorithm, (c) logarithm of the relative error on the magnitude of the magnetic flux density, (d) logarithm of the Frobenius norm of the total displacement, as functions of components B_x and B_y of the magnetic flux density, with icosphere of order 4.

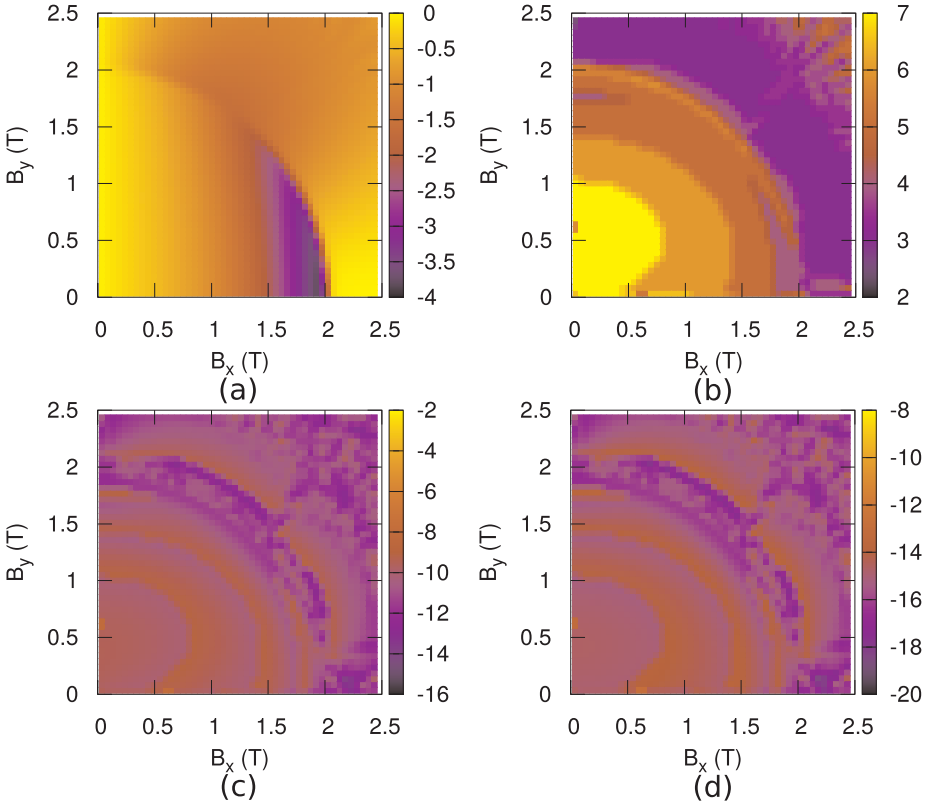

Fig. 9. Maps of (a) $(\partial_\epsilon \vec{H})_{xxx}$ (10^6 A/m), (b) number of converging iterations of the Newton–Raphson algorithm, (c) logarithm of the relative error on the magnitude of the magnetic flux density, (d) logarithm of the Frobenius norm of the total displacement, as functions of components B_x and B_y of the magnetic flux density, with icosphere of order 6.

configuration would turn out to be a parallel traction/orthogonal compression when the magnetic field rotates $\pi/4$ rad (in a 2D configuration). From these considerations, the differentiation and integration of the analytical SMSM may be more conveniently performed numerically. The inversion may also be performed using algorithms that do not need the evaluation of derivatives.

4. Association with Jiles-Atherton magnetic hysteresis model

The original Jiles-Atherton (JA) approach [36] was already extended to consider some anisotropy and texture effects by using a generalized anhysteretic magnetization [37,38]. Here, a SMSM is used to provide a description of the anhysteretic magneto-elastic behaviour and, hence, to include anistropy, texture and mechanical stress effects. A vector extension of JA model, as proposed in [39], is defined by the magnetization increment which can be expressed as

$$d\vec{M}_{hys} = \chi_f \, d\vec{H}_e + c \, d\vec{M} \tag{46}$$

The effective magnetic field is $\vec{H}_e = \vec{H} + \beta\vec{M}_{hys}$, and $\vec{M}$ is an anhysteretic component function of $\vec{H}_e$. The tensor χ_f is defined by:if $\vec{\chi}_f . \, d\vec{H}_e > 0$,

$$\chi_f = |\vec{\chi}_f|^{-1}\vec{\chi}_f \otimes \vec{\chi}_f \tag{47}$$

else,

$$\chi_f = \mathbf{0} \tag{48}$$

where $\vec{\chi}_f = \frac{1}{k}(\vec{M} - \vec{M}_{hys})$. As shown in [40], an explicit expression of the hysteretic differential susceptibility is then

$$\chi = \frac{d\vec{M}_{hys}}{d\vec{H}} = (\boldsymbol{I} - \beta(\chi_f + c\chi_{an}))^{-1}(\chi_f + c\chi_{an}) \tag{49}$$

From this, the direct JA model can be built by numerical integration. Similarly, the inverse JA model can be built from

$$\xi = \mu_0 \frac{d\vec{M}_{hys}}{d\vec{B}} = (\boldsymbol{I} - (\beta - 1)(\chi_f + c\chi_{an}))^{-1}(\chi_f + c\chi_{an}). \tag{50}$$

It can be noticed that, if c and β are scalar, then

$$\chi^{-1} = (\chi_f + c\chi_{an})^{-1} - \beta\boldsymbol{I} \tag{51}$$

and this tensor is symmetrical if χ_{an} is also symmetrical. This property is interesting for an application in the finite element method but it is not a necessary condition for hysteretic materials.

The anhysteretic magnetization and differential susceptibility can be obtained from a SMSM in order to account for the applied mechanical stress. Considering the effective field $\vec{H}_e$ and the constant applied stress σ_0 as input parameters, we have:

$$\vec{M}_{an} = \vec{M}(\vec{H}_e, \sigma_0) \tag{52}$$

$$\chi_{an} = \frac{d\vec{M}}{d\vec{H}_e}(\vec{H}_e, \sigma_0) \tag{53}$$

If the macroscopically equivalent crystal SMSM is used with $W_\alpha^{an} = 0$ and $\sigma_0 = \mathbf{0}$, the obtained magnetization is the same as the one given by the usual Langevin function (except for numerical differences due to integrals evaluation) and the JA model "a" parameter is related to the "A_s" parameter of the SMSM by

$$A_s = \frac{1}{\mu_0 M_s a}. \tag{54}$$

The introduction of the SMSM in JA model allows to account for the effect of multiaxial stress on the steepness of the loop. However, it may not be sufficient to describe the effect of stress on the shape of the hysteresis loops and on the losses. One possible solution consists in considering variations of the so-called pinning parameter k, which is strongly related to hysteresis losses [2].

Here we consider the parameter k constant and we focus on the magnetostriciton hysteresis under a constant applied stress (σ_0). We define an anhysteretic magnetic field ($\vec{H}_{an}$) such that the corresponding output of the SMSM is equal to the output of the hysteretic model:

$$\vec{M}_{hys}(\vec{H}, \sigma_0) = \vec{M}(\vec{H}_{an}, \sigma_0) \tag{55}$$

Dropping the constant parameter σ_0, the differential of the magnetization is:

$$d\vec{M}_{hys}(\vec{H}) = \frac{d\vec{M}}{d\vec{H}_{an}}(\vec{H}_{an}) d\vec{H}_{an}(\vec{H}) \tag{56}$$

In this equation $\frac{d\vec{M}}{d\vec{H}_{an}}(\vec{H}_{an}) = \chi_{an}$ is the anhysteretic differential susceptibility calculated from the SMSM model at the current value of $\vec{H}_{an}$. $\vec{H}_{an}$ can be obtained by integration of

$$d\vec{H}_{an} = \chi_{an}^{-1} \, d\vec{M}_{hys}. \tag{57}$$

The hysteretic magnetostriction is obtained (together with χ_{an}) from the SMSM model by

$$\varepsilon_{hys}^{\mu}(\vec{H}, \sigma_0) = \varepsilon^{\mu}(\vec{H}_{an}, \sigma_0) \tag{58}$$

This procedure can be applied identically to the direct or inverse version of the JA-SMSM.

The same non-oriented Fe-3%Si material as in Section 2.3 is considered as an example of hysteretic magneto-elastic behaviour. The parameters of the JA part of the model are given in Table 3. The hysteresis loops obtained for magnetization and magnetostriction in the direction of the applied magnetic field for different values of stress are shown in Fig. 10. These curves are in good accordance with the experimental results [32]. Despite the discrepancies that appear when comparing experimental and modelled behaviour for a particular value of the mechanical stress, the model shows a good consistency considering the loop shapes and evolution trends. The experimental data available for a particular material is generally limited to this kind of uniaxial mechanical stress/magnetic field characteristics. On the contrary, the JA-SMSM is fully multi-axial and can be applied to any magneto-elastic loading configuration. However, experimental tests with biaxial stress and/or rotating magnetic flux density should be done in order to check the consistency and accuracy of the model predictions.

5. Application to device simulation

The TEAM workshop problem 32 [28] presents a three-limbed magnetic core structure with two windings and different operating conditions (Fig. 11). This problem offers interesting characteristics for testing magnetic field analysis tools. Here, FreeFem++ [41] is used to solve the problem with the finite element method. In figure 11 the proportions of the true device are not respected. The true core structure has an almost square external frame of 175 mm side length. The width of the limbs is 30 mm. The model is developed here in 2D and extended in order to make possible the application of stress on the core structure and to simulate its influence on the magnetic field and magnetostriction distribution. The core structure is assumed to be under vertical (i.e. in the limbs direction) compressive conditions corresponding to an imposed vertical displacement on the upper side, a null y-displacement on the lower side, and a null x-displacement at the lower left corner

Table 3
Jiles-Atherton parameters for the non-oriented Fe-3%Si material.

β	k (A/m)	c
10^{-4}	200	0.4

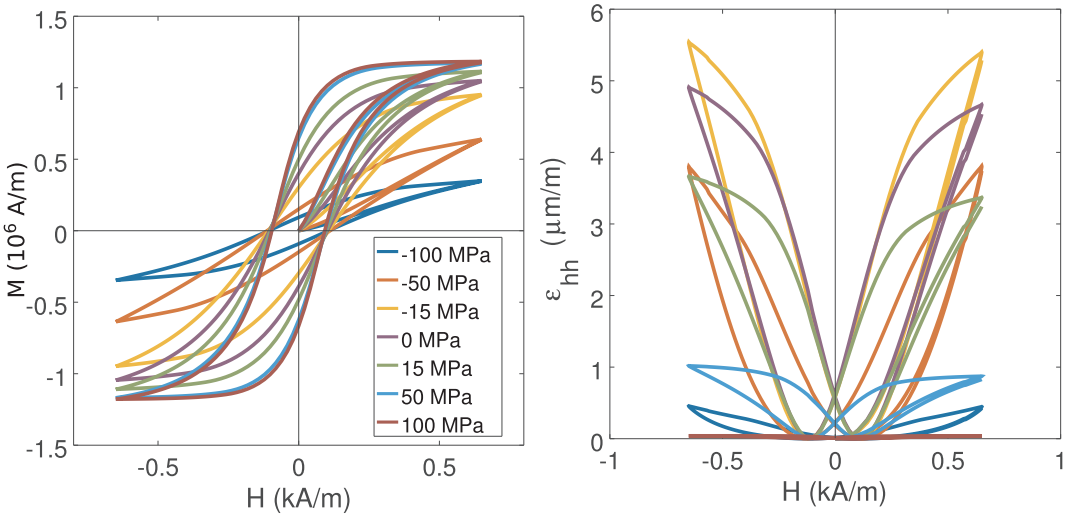

Fig. 10. Hysteresis loops for the magnetization and magnetostriction as a function of the magnetic field under unixial stress.

(Fig. 11). The resulting mechanical stress is computed using the finite element method and with the help of FreeFem++ [41]. A usual displacement ($\vec{u}$) formulation of the plane stress static elasticity problem is considered. The discretized weak form of the problem is summarized by the following equations:

$$\int_{\Omega_C} \boldsymbol{\sigma} : grad_s\, \vec{v}_{ij}\, d\Omega_C = 0 \tag{59}$$

$$\boldsymbol{\sigma} = \boldsymbol{C} : grad_s\, \vec{u} \tag{60}$$

$$\vec{u} = \Sigma_{i=1}^{N_C} \Sigma_{j=1}^{2} \mathrm{u}_{ij}\, \vec{v}_{ij} \tag{61}$$

where Ω_C is the core region, $\vec{v}_{ij}$ are the vectorial nodal test and interpolation functions in direction j at node i, $grad_s$ is the symmetrical gradient operator, $\boldsymbol{C}$ is the fourth-order stiffness tensor, u_{ij} is the degree of freedom for the j-component of the displacement at node i, and N_C is the number of nodes of the core part of the mesh. The elastic properties of the material are assumed isotropic (Young's modulus $E = 210\,GPa$ and Poisson's coefficient $\nu = 0.29$). For an imposed displacement of $-40\mu m$, Fig. 12 presents the distribution of xx- and yy- components of the stress. The shear stress (xy-component) is not shown but is smaller (less than $13MPa$) and concentrated near internal corners.

Neglecting the stress induced by magnetostriction, the magnetic problem is then solved considering a constant applied stress. Tangential magnetic field conditions are considered on the external boundary of the computational domain (Fig. 11). The external boundary is 45 mm distant from the core. By comparison with the reference results of [28], the relative proximity of this boundary did not show significant impact on simulations (leakage flux is small in this application). A time-stepping forward Euler scheme is used. At each time step, the solution increment is firstly computed considering the fully linearised problem (differential permeability or reluctivity [42,43]), and then a non-linear Newton–Raphson iteration might be applied. The voltage source (V_i) and series resistance $R_s = 11.1\Omega$ connected to coil i are coupled to the magnetic finite element model by the circuit equation which leads to the definition of the following residual:

$$\mathscr{R}^{ci} = V_i - \frac{e}{\Delta t}(\Phi_i - \Phi_i^0) - R_s I_i \tag{62}$$

for $i \in \{1, 2\}$, where e is the thickness of the core, I_i is the current in the coil, Δt is the value of the time step, Φ_i and Φ_i^0 are the total magnetic flux in the coil per unit length at current and former time step, respectively. For the magnetic vector potential formulation, the residual relative to the finite element model is

$$\mathscr{R}_i^A = \int_\Omega \vec{H} \cdot rot\, \vec{w}_i^1\, d\Omega - \int_\Omega \vec{J} \cdot \vec{w}_i^1\, d\Omega \tag{63}$$

where Ω is the whole computational domain, $\vec{w}_i^1$ is the vector (parallel to z-direction) nodal test function and $\vec{J}$ is the electric current density. For the magnetic scalar potential formulation, the residual relative to the finite element model is

$$\mathscr{R}_i^\phi = \int_\Omega \vec{B} \cdot grad\, w_i^0\, d\Omega \tag{64}$$

where w_i^0 is the scalar nodal test function for node i. The magnetic field of Eq. (63) is related to the magnetic vector potential ($\vec{A}$) by

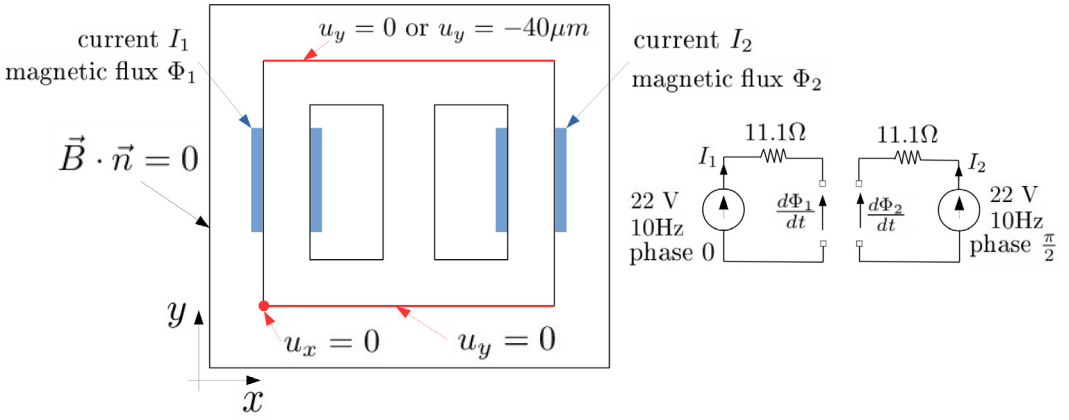

Fig. 11. Scheme of the transformer with boundary and finite elements/circuit coupling conditions.

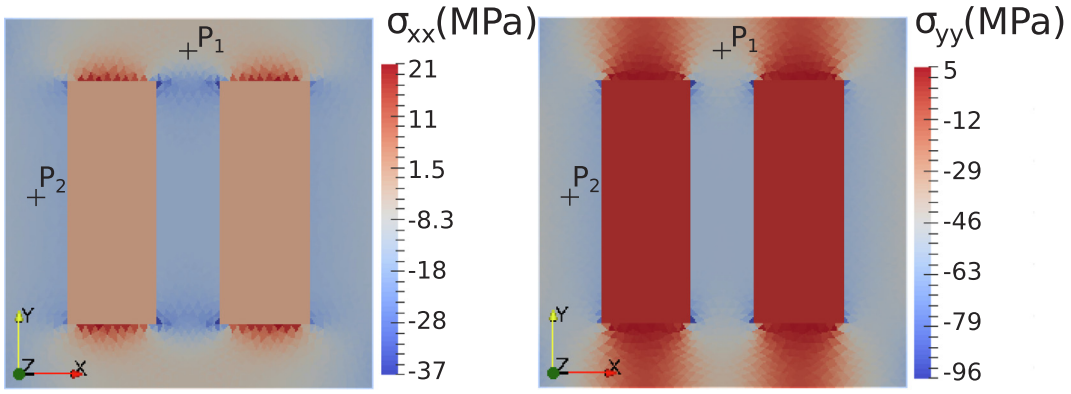

Fig. 12. Distribution of stress.

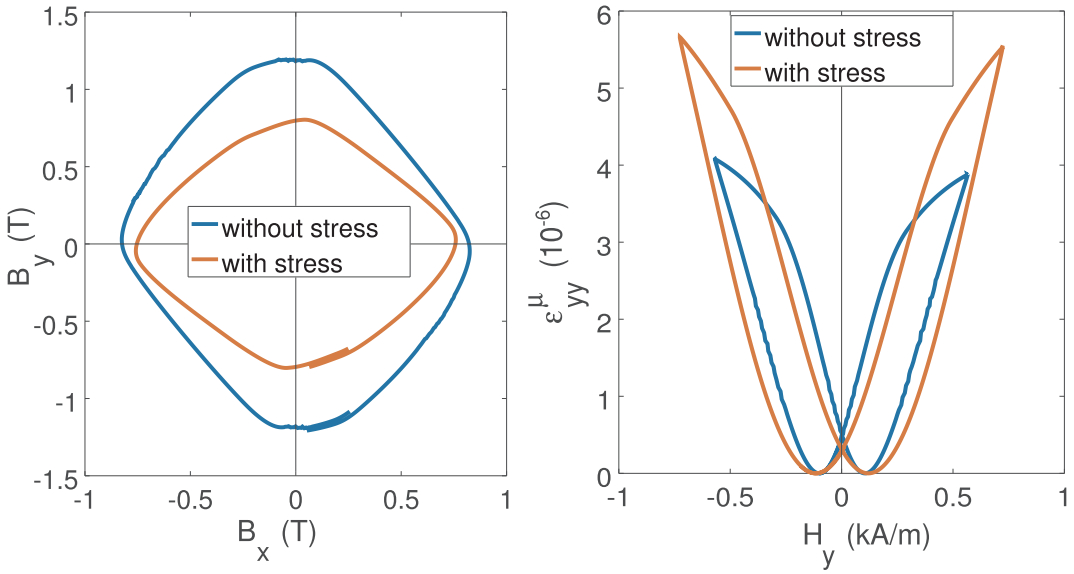

Fig. 13. Effect of stress on induction in the upper T-joint (left) and magnetostriction at the center of left limb (right).

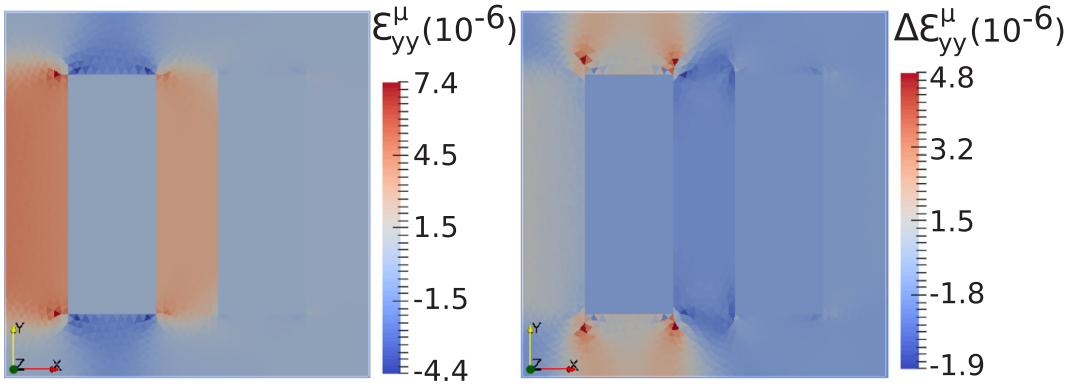

Fig. 14. Effect of stress on the distribution of the *yy*-component of the magnetostriction.

$$\vec{H} = \nu_0 \, rot \, \vec{A} - \vec{M}_{hys} \tag{65}$$

and the magnetic flux density of Eq. (64) is related to the scalar magnetic potential ϕ by

$$\vec{B} = \mu_0 (\vec{T} - grad\,\phi + \vec{M}_{hys}) \tag{66}$$

where $\vec{T}$ is a magnetic source field which verifies $rot\,\vec{T} = \vec{J}$. In terms of the unknown currents (I_i), we have

$$\vec{J} = \Sigma_{i=1}^{2} I_i \vec{J}_i^{\,n} \tag{67}$$

and

$$\vec{T} = \Sigma_{i=1}^{2} I_i \vec{T}_i^{\,n} \tag{68}$$

where $\vec{J}_i^{\,n}$ and $\vec{T}_i^{\,n}$ are constant normalized vector fields imposed by the coils geometry. These fields are also used to express the total flux in each coil per unit length, from the unknows,

$$\Phi_i = \int_\Omega \vec{A} \cdot \vec{J}_i^{\,n} \, d\Omega \tag{69}$$

or

$$\Phi_i = \int_\Omega \vec{B} \cdot \vec{T}_i^{\,n} \, d\Omega \tag{70}$$

depending on the formulation. The discretized scalar potential and magnetic potential are

$$\phi = \Sigma_{i=1}^{N} p_i w_i^0 \tag{71}$$

and

$$\vec{A} = \Sigma_{i=1}^{N} a_i \vec{w}_i^1 \tag{72}$$

respectively, where p_i and a_i are the corresponding degrees of freedom and N is the total number of nodes. Linearisation or application of the Newton-Raphson procedure involves the differentiation of the residuals with respect to the unknowns. In particular, the Jacobian matrix includes the following derivatives, obtained by the chain rule:

$$\frac{\partial \vec{H}}{\partial a_j} = \frac{d\vec{H}}{d\vec{B}} \frac{\partial \vec{B}}{\partial a_j} = \nu_0 (\boldsymbol{I} - \boldsymbol{\xi}) rot \, \vec{w}_j^1 \tag{73}$$

$$\frac{\partial \vec{B}}{\partial p_j} = \frac{d\vec{B}}{d\vec{H}} \frac{\partial \vec{H}}{\partial p_j} = \mu_0 (\boldsymbol{I} + \boldsymbol{\chi}) grad \, w_j^0 \tag{74}$$

where $\boldsymbol{\xi}$ and $\boldsymbol{\chi}$ are given by the JA-SMSM presented in Section 4. For the non-linear iteration, the material behaviour is evaluated using an adaptive number of substeps (determined by a fixed sub-increment of the applied field). An adaptive relaxation is also applied using the technique presented in [44,45].

The configuration of the TEAM workshop problem 32 case 3 (Fig. 11) is chosen because it creates regions with rotational field (in the so-called T-joint regions) but no minor loops (not well represented by the JA model). In the T-joints, the rotational characteristic of the magnetization and the associated magnetostriction may also have significant effects on the total strain [4]. The peak value of the voltage on the coils is set to 22 V in order to reach an induction of around 1.3 T in the limbs, considering the material properties modelled as presented in Section 4 when no stress is applied. It should be noticed that each coil is connected to a voltage source through a series resistor of relatively large value (11.1Ω). At the considered frequency (10 Hz), these resistors lead the transformer to operate as a current fed one.

The magnetostatic formulations in terms of magnetic reduced scalar potential and vector potential were tested. The reduced scalar potential formulation showed a good stability of the time-stepping resolution using the fully linearised approach, but the application of the non-linear resolution algorithm led to divergence in most cases. This might be due to problems of accuracy of the solution using the reduced scalar potential with source field inside the magnetic material [46]. On the other hand, the vector potential formulation showed a poor stability when using the fully linearised approach, but the application of the non-linear resolution algorithm had good convergence properties and stabilized the time-stepping scheme. Here, only the results obtained with the vector potential formulation are presented.

After a magnetizing phase, the system is simulated for one period of the voltage on the coils. Fig. 13 shows the locus of the magnetic induction for a point in the upper T-joint and the *yy*-component of the magnetostriction for a point in the middle of the left limb (P_1 and P_2, respectively, shown in Fig. 12). The curves corresponding to the cases without mechanical stress and with the mechanical stress computed before are presented. At the considered point in the T-joint, the stress is mainly compressive in the *y*-direction which modifies the rotation of the induction reducing the *y*-component variations. At the considered point in the left limb, the stress is mainly compressive in the direction of the magnetic field, which results in a greater *yy*-component of the magnetostriction. Finally, the distribution of the *yy*-component of the magnetostriction for the last time step of the simulation (corresponding to a maximum value of the left coil voltage) considering the stress is shown in Fig. 14 together with the difference with the no-stress case. It is shown that the applied stress strongly modifies the magnetostriction distribution.

6. Conclusion

The simplified multiscale models are shown to be flexible and robust tools for the representation of magneto-elastic couplings in device analysis. From a small set of material parameters, the models are able to give physically representative results for a wide range of applied loadings(Figs. 5–7). In terms of numerical evaluation, the robustness of the model principally depends on the chosen discretization parameters (e.g. icosphere order, number of time-steps for the association with Jiles-Atherton model). These parameters should be defined according to each specific application, finding a good compromise between numerical robustness and computational cost. The finite element application example shows that magnetic field simulations can be performed considering applied stress and rotational magnetic field region. Convergence problems were encountered, but consistent simulation results could be obtained with both scalar and vector potential formulations. This type of problems associated with hysteretic magnetic field simulations are commonly reported in the literature using other types of material behavior models. Thus, the proposed models constitute possible alternatives with their specific strengths. The complexity (in terms of physical representativeness and numerical evaluation) of the model can be easily adapted to the needs of a particular application and the physical consistency of the results is provided by the approach based on the energy balance of the material. All the features needed for the application of such models in magnetic field analysis tools are detailed. With these tools, the SMSMs offer new possibilities for the analysis of the effect of multiaxial mechanical stress on electromagnetic devices and for the analysis of magneto-mechanical transducers based on magneto-elastic couplings.

Acknowledgement

This research was partially funded by the CAPES/MEC Brazilian agency.

References

[1] N. Takahashi, H. Morimoto, Y. Yunoki, D. Miyagi, Effect of shrink fitting and cutting on iron loss of permanent magnet motor, J. Magn. Magn. Mater. 320 (20) (2008) e925–e928.
[2] L. Bernard, L. Daniel, Effect of stress on magnetic hysteresis losses in a switched reluctance motor: application to stator and rotor shrink fitting, IEEE Trans. Magn. 51 (9) (2015) 1–13.
[3] X. Mininger, N. Galopin, X. Ojeda, F. Bouillault, M. Gabsi, Modeling of magnetoelastic and piezoelectric coupling: application to srm noise damping, IEEE Trans. Magn. 45 (3) (2009) 1218–1221.
[4] C. Krell, N. Baumgartinger, G. Krismanic, E. Leiss, H. Pfützner, Relevance of multidirectional magnetostriction for the noise generation of transformer cores, J. Magn. Magn. Mater. 215 (2000) 634–636.
[5] M. Liu, O. Hubert, X. Mininger, F. Bouillault, L. Bernard, Homogenized magnetoelastic behavior model for the computation of strain due to magnetostriction in transformers, IEEE Trans. Magn. 52 (2) (2016) 1–12.
[6] T. Ueno, T. Higuchi, Two-dof micro magnetostrictive bending actuator for wobbling motion, IEEE Trans. Magn. 44 (11) (2008) 4078–4080.
[7] T. Zhang, C. Jiang, H. Zhang, H. Xu, Giant magnetostrictive actuators for active vibration control, Smart Mater. Struct. 13 (3) (2004) 473.
[8] F.T. Calkins, A.B. Flatau, M.J. Dapino, Overview of magnetostrictive sensor technology, J. Intell. Mater. Syst. Struct. 18 (10) (2007) 1057–1066.
[9] T.T. Nguyen, F. Bouillault, L. Daniel, X. Mininger, Finite element modeling of magnetic field sensors based on nonlinear magnetoelectric effect, J. Appl. Phys. 109 (8) (2011) 084904 .
[10] G. Krebs, L. Daniel, Giant magnetostrictive materials for field weakening: a modeling approach, IEEE Trans. Magn. 48 (9) (2012) 2488–2494.
[11] M.J. Sablik, H. Kwun, G.L. Burkhardt, D.C. Jiles, Model for the effect of tensile and compressive stress on ferromagnetic hysteresis, J. Appl. Phys. 61 (8) (1987) 3799–3801.

[12] M. Sablik, H. Kwun, G. Burkhardt, Biaxial stress effects on hysteresis and mivc, J. Magn. Magn. Mater. 140 (1995) 1871–1872.
[13] D. Singh, F. Martin, P. Rasilo, A. Belahcen, Magnetomechanical model for hysteresis in electrical steel sheet, IEEE Trans. Magn. 52 (11) (2016) 1–9.
[14] A. Benabou, L. Vandenbossche, J. Gyselinck, S. Clenet, L. Dupré, P. Dular, Inclusion of a stress-dependent preisach model in 2d fe calculations, COMPEL – Int. J. Comput. Math. Electr. Electron. Eng. 25 (1) (2006) 81–90.
[15] F. Ossart, L. Hirsinger, R. Billardon, Computation of electromagnetic losses including stress dependence of magnetic hysteresis, J. Magn. Magn. Mater. 196 (1999) 924–926.
[16] V. Permiakov, L. Dupré, A. Pulnikov, J. Melkebeek, Loss separation and parameters for hysteresis modelling under compressive and tensile stresses, J. Magn. Magn. Mater. 272 (2004) E553–E554.
[17] M. Rekik, O. Hubert, L. Daniel, Influence of a multiaxial stress on the reversible and irreversible magnetic behaviour of a 3%Si-Fe alloy, Int. J. Appl. Electromagnet Mech. 44 (3–4) (2014) 301–315.
[18] U. Aydin, P. Rasilo, F. Martin, A. Belahcen, L. Daniel, A. Haavisto, A. Arkkio, Effect of multi-axial stress on iron losses of electrical steel sheets, J. Magn. Magn. Mater. 469 (2019) 19–27.
[19] U. Aydin, F. Martin, P. Rasilo, A. Belahcen, A. Haavisto, D. Singh, L. Daniel, A. Arkkio, Rotational single sheet tester for multiaxial magneto-mechanical effects in steel sheets, IEEE Trans. Magn. 55 (3) (2019) 2001810.
[20] W.D. Armstrong, An incremental theory of magneto-elastic hysteresis in pseudo-cubic ferro-magnetostrictive alloys, J. Magn. Magn. Mater. 263 (1–2) (2003) 208–218.
[21] U. Aydin, P. Rasilo, F. Martin, D. Singh, L. Daniel, A. Belahcen, M. Rekik, O. Hubert, R. Kouhia, A. Arkkio, Magneto-mechanical modeling of electrical steel sheets, J. Magn. Magn. Mater. 439 (2017) 82–90.
[22] N. Buiron, L. Hirsinger, R. Billardon, A multiscale model for magneto-elastic couplings, J. Phys. IV 9 (1999) 187.
[23] L. Daniel, O. Hubert, R. Billardon, Homogenisation of magneto-elastic behaviour: from the grain to the macro scale, Comput. Appl. Math. 23 (2–3) (2004) 285–308.
[24] L. Daniel, O. Hubert, N. Buiron, R. Billardon, Reversible magneto-elastic behavior: a multiscale approach, J. Mech. Phys. Solids 56 (3) (2008) 1018–1042.
[25] L. Daniel, M. Rekik, O. Hubert, A multiscale model for magneto-elastic behaviour including hysteresis effects, Arch. Appl. Mech. 84 (9) (2014) 1307–1323.
[26] D. Vanoost, S. Steentjes, J. Peuteman, G. Gielen, H. De Gersem, D. Pissoort, K. Hameyer, Magnetic hysteresis at the domain scale of a multi-scale material model for magneto-elastic behaviour, J. Magn. Magn. Mater. 414 (2016) 168–179.
[27] L. Bernard, X. Mininger, L. Daniel, G. Krebs, F. Bouillault, M. Gabsi, Effect of stress on switched reluctance motors: a magneto-elastic finite-element approach based on multiscale constitutive laws, IEEE Trans. Magn. 47 (9) (2011) 2171–2178.
[28] O. Bottauscio, M. Chiampi, C. Ragusa, L. Rege, R. Maurizio, Description of team problem: 32 a–test case for validation of magnetic field analysis with vector hysteresis, [online] Available: http://www.compumag.org/jsite/images/stories/TEAM/Problem32.pdf and http://www.cadema.polito.it/.
[29] L. Daniel, N. Galopin, A constitutive law for magnetostrictive materials and its application to Terfenol-D single and polycrystals, Eur. Phys. J. Appl. Phys. 42 (02) (2008) 153–159.
[30] L. Daniel, An analytical model for the effect of multiaxial stress on the magnetic susceptibility of ferromagnetic materials, IEEE Trans. Magn. 49 (5) (2013) 2037–2040.
[31] L. Daniel, An analytical model for the magnetostriction strain of ferromagnetic materials subjected to multiaxial stress, Eur. Phys. J. Appl. Phys. 83 (3) (2018) 30904.
[32] M. Rekik, Mesure et modélisation du comportement magnéto-mécanique dissipatif des matériaux ferromagnétiques à haute limite élastique sous chargement multi-axial, Ph.D. thesis, École normale supérieure de Cachan-ENS Cachan, 2014.
[33] O. Perevertov, Influence of the applied elastic tensile and compressive stress on the hysteresis curves of fe-3% si non-oriented steel, J. Magn. Magn. Mater. 428 (2017) 223–228.
[34] L. Bernard, B.J. Mailhé, N. Sadowski, L. Daniel, Differential model of magneto-elastic behaviour based on a multi-scale approach, MOMAG 2016 (17th Simpôsio Brasileiro de Micro-ondas e Optoeletrônica and 12th Congresso Brasileiro de Eletromagnetismo).
[35] L. Bernard, B.J. Mailhé, N. Sadowski, L. Daniel, Numerical inversion of a 2-scale magneto-elastic behaviour model, COMPUMAG 2017 (21st International Conference on the Computation of Electromagnetic Fields).
[36] D.C. Jiles, D.L. Atherton, Theory of ferromagnetic hysteresis, J. Magn. Magn. Mater. 61 (1–2) (1986) 48–60.
[37] Y. Shi, D. Jiles, A. Ramesh, Generalization of hysteresis modeling to anisotropic and textured materials1, J. Magn. Magn. Mater. 187 (1) (1998) 75–78.
[38] D. Jiles, Hysteresis models: non-linear magnetism on length scales from the atomistic to the macroscopic, J. Magn. Magn. Mater. 242 (2002) 116–124.
[39] A. Bergqvist, A simple vector generalization of the Jiles-Atherton model of hysteresis, IEEE Trans. Magn. 32 (5) (1996) 4213–4215.
[40] J.V. Leite, N. Sadowski, P. Kuo-Peng, N.J. Batistela, J.P.A. Bastos, A.A. de Espíndola, Inverse Jiles-Atherton vector hysteresis model, IEEE Trans. Magn. 40 (4) (2004) 1769–1775.
[41] F. Hecht, New development in freefem + +, J. Numer. Math. 20 (3–4) (2012) 251–266.
[42] J. Bastos, N. Sadowski, A new formulation using differential permeability based on the source-field method, IEEE Trans. Magn. 46 (8) (2010) 3369–3372.
[43] J.P.A. Bastos, N. Sadowski, J.V. Leite, N.J. Batistela, K. Hoffmann, G. Meunier, O. Chadebec, A differential permeability 3-d formulation for anisotropic vector hysteresis analysis, IEEE Trans. Magn. 50 (2) (2014) 341–344.
[44] K. Fujiwara, T. Nakata, N. Okamoto, K. Muramatsu, Method for determining relaxation factor for modified newton-raphson method, IEEE Trans. Magn. 29 (2) (1993) 1962–1965.
[45] C. Guérin, K. Jacques, R.V. Sabariego, P. Dular, C. Geuzaine, J. Gyselinck, Using a jiles-atherton vector hysteresis model for isotropic magnetic materials with the finite element method, newton-raphson method, and relaxation procedure, Int. J. Numer. Modelling: Electron. Networks Devices Fields 30 (5) (2017) e2189 .
[46] J. Simkin, C. Trowbridge, On the use of the total scalar potential on the numerical solution of fields problems in electromagnetics, Int. J. Numer. Meth. Eng. 14 (3) (1979) 423–440.